

Discovery of multiple Lorentzian components in the X-ray timing properties of the Narrow Line Seyfert 1 Ark 564

I. M. McHardy^{1*}, P. Arévalo¹, P. Uttley¹, I. E. Papadakis², D. P. Summons¹,
W. Brinkmann³, M. J. Page⁴

¹*School of Physics and Astronomy, University of Southampton, Southampton SO17 1BJ, UK*

²*Physics Department, University of Crete, P.O.Box 2208, 71003 Heraklion, Greece*

³*Max-Planck-Institut für extraterrestrische Physik, Giessenbachstrasse, 85741 Garching, Germany*

⁴*Mullard Space Science Laboratory, University College London, Holmbury St Mary, Dorking, RH5 6NT*

Received / Accepted

ABSTRACT

We present a power spectral analysis of a 100 ksec *XMM-Newton* observation of the narrow line Seyfert 1 galaxy Ark 564. When combined with earlier *RXTE* and *ASCA* observations, these data produce a power spectrum covering seven decades of frequency which is well described by a power law with two very clear breaks. This shape is unlike the power spectra of almost all other AGN observed so far, which have only one detected break, and resemble Galactic binary systems in a soft state. The power spectrum can also be well described by the sum of two Lorentzian-shaped components, the one at higher frequencies having a hard spectrum, similar to those seen in Galactic binary systems. Previously we have demonstrated that the lag of the hard band variations relative to the soft band in Ark 564 is dependent on variability time-scale, as seen in Galactic binary sources. Here we show that the time-scale dependence of the lags can be described well using the same two-Lorentzian model which describes the power spectrum, assuming that each Lorentzian component has a distinct time lag. Thus all X-ray timing evidence points strongly to two discrete, localised, regions as the origin of most of the variability. Similar behaviour is seen in Galactic X-ray binary systems in most states other than the soft state, i.e. in the low-hard and intermediate/very high states. Given the very high accretion rate of Ark 564 the closest analogy is with the very high (intermediate) state rather than the low-hard state. We therefore strengthen the comparison between AGN and Galactic binary sources beyond previous studies by extending it to the previously poorly studied very high accretion rate regime.

Key words: Galaxies: active, powerspectra: Lorentzian components, accretion: discs, spectral timing: phase lags

1 INTRODUCTION

Understanding the relationship between AGN, which are powered by accretion onto supermassive black holes, and the stellar mass Galactic black hole binary systems (GBHs) is currently one of the major research areas in high energy astrophysics. If we can understand the relationship, then we can predict how AGN should behave on cosmological time-

scales by observing the brighter, and much faster varying, GBHs.

The comparison is complicated by the fact that (at the risk of some oversimplification), GBHs can exist in a number of states, defined originally in terms of their medium energy (2–10 keV) X-ray properties, particularly: (i) the hard spectrum, low-flux (‘hard’) state, (ii) the soft spectrum, high flux (‘soft’) state and (iii) the ‘very high state’ (VHS - sometimes also described as the high-intermediate state) where the flux is very high and the spectrum very soft. In general the accretion rate increases as we go from

* E-mail: imh@astro.soton.ac.uk

the hard to soft to VHS states. See Remillard & McClintock (2006) for a comprehensive description of GBH states and behaviour.

The various states have quite distinct X-ray timing properties which may, in fact, provide a more fundamental state discriminator than the spectral properties. Timing is usually quantified in terms of the power spectral densities (PSDs) of the X-ray lightcurves. Where significant variability is observed, ‘soft’ state PSDs are characterised by a power law of slope of -1 at low frequencies (i.e. the power, $P(\nu) \propto \nu^{-\alpha}$ with $\alpha \sim 1$), breaking to a slope $\alpha \geq 2$ above a characteristic frequency ν_B (or time-scale T_B). Hard state and VHS state GBH PSDs, which are similar to each other, are more complex. They are best described by the combination of two or more Lorentzian-shaped components (e.g. Nowak 2000), although at low signal to noise they can be approximated by a power law with a second, lower frequency break, approximately 1.5 to 2 decades lower in frequency than the high frequency break.

So far, almost all well observed AGN, which are X-ray bright and have moderately high accretion rates, have soft state PSDs, as we would expect from comparison with GBHs of similar accretion rate (measured relative to the Eddington accretion rate, \dot{m}_E) (e.g. McHardy et al. 2004, 2005; Uttley & McHardy 2005). However the comparison for the hard and VHS states is largely unknown. Until very recently, NGC3783 had been suggested to have two breaks in its PSD (Markowitz et al. 2003) and so be a hard state AGN, although its accretion rate is similar to that of the well observed soft state AGN. However recent work, based on improved data (Summons et al. 2007), has shown that, in fact, NGC3783 is another soft state AGN. If soft states are linked to the accretion disc extending in to very small radii, then perhaps their much cooler accretion discs compared to GBHs may allow the optically thick disc to survive without evaporation to smaller radii. Thus maybe all AGN are soft state objects and the comparison with GBHs does not extend to other states? Such a conclusion would have a fundamental impact on our understanding of the accretion process onto black holes and so it is very important to confirm, from timing properties, a definite non-soft state AGN.

The only remaining case where there is at least some evidence for a non-soft state PSD is Ark 564. From observations with *RXTE*, evidence for a low frequency break in the PSD was presented by Pounds et al. (2001). Evidence for a second break, at high frequencies, was presented by Papadakis et al. (2002) from analysis of *ASCA* observations. Papadakis et al. (2002) interpreted the combined *RXTE* and *ASCA* PSD as a hard state PSD but did note that the high frequency break does not scale linearly with mass to the hard state of the archtypal GBH Cyg X-1; the frequency difference is too small. However as Ark 564 is one of the highest accretion rate AGN known ($\dot{m}_E \sim 1$, Romano et al. (2004)), a VHS state remains a strong possibility.

Unfortunately proper modelling of the combined long and short time-scale PSD is hampered by the gaps which occur in the *ASCA* light curves, and hence in the PSD, at

the orbital period (~ 5600 s). We therefore made a 100 ks continuous observation with *XMM-Newton* to fill that gap in the PSD. Spectral analysis of this *XMM-Newton* observation has been presented by Papadakis et al. (2007) and Brinkmann et al. (2007) and cross-spectral analysis (i.e. lags between energy bands as a function of Fourier frequency or time-scale) has been presented by Arévalo et al. (2006).

Here we present a full power spectral analysis of the combined *RXTE*, *ASCA* and *XMM-Newton* data and find firm evidence for two breaks in the combined PSD. We also show that the PSD can be parameterised as the sum of two Lorentzian components. We note particularly that the highest frequency Lorentzian, for which good spectral information is available from both the *XMM-Newton* and *ASCA* observations, is stronger at higher energies, exactly as is found for Lorentzian components in GBHs. In GBHs in the hard and VHS states, changes in the lag between bands occur at approximately the time-scales at which the PSD changes from one Lorentzian component to another, supporting the model that each Lorentzian comes from a separate physical emission region. In this paper we therefore re-examine the lag spectrum and compare it with the PSD, to test whether a two-component emission region may apply in Ark 564 and also as a further diagnostic of the state of the AGN.

The paper is arranged as follows: In Sec. 2, we describe the observational data sets which we used and discuss the individual *ASCA* and *XMM-Newton* PSDs in Secs 3 and 4. We then discuss the joint *RXTE* *ASCA* and *XMM-Newton* power spectrum and its energy dependence in Sec. 5 and compare the powerspectrum with the lag spectrum in Sec 6. We summarise our conclusions in Sec. 7.

2 SUMMARY OF OBSERVATIONS

2.1 *RXTE*

Ark 564 was observed by *RXTE* from 1999 January 1 to 2003 March 4. For most of this period observations were carried out approximately once every 4 days but from 2000 May 31 to 2000 July 01, observations were carried out 8 times per day. The observations from 1999 January 1 to 2000 September 19 are described in detail in Pounds et al. (2001). We have extracted all of the *RXTE* data from the archive and produced 2–10 keV lightcurves in the same manner as we have described for other *RXTE* AGN monitoring programmes (e.g. see McHardy et al. 2004, for details). For use in power spectral analysis we produce a long time-scale light curve, covering the full observing period with 4-day sampling, and an intermediate time-scale lightcurve, covering the one month period of 3-hour sampling.

2.2 *ASCA*

Ark 564 was monitored with *ASCA* between 2000 June 1 and July 5, producing a month-long light curve. This observation was only interrupted by the regular Earth occultations of the satellite on the orbital time-scale of 5632s. Binning the data in orbit-long bins produces an evenly sampled light curve, containing 551 points, that probes time-scales

from a few times 10^6 to 10^4 s. Additionally, each of the 551 individual orbits cover time-scales of $10^3 - 10^2$ s, whose power spectra can be combined to produce a high quality high frequency PSD.

We downloaded SIS data from the TARTARUS database in 0.6–2 and 2–10 keV energy bands and produced background subtracted light curves, with average count rates of 2.7 and 0.6 c/s respectively. The average photon energies of these two bands are 1.18 and 3.2 keV respectively.

The lightcurves, PSD and other variability properties of this data set have been studied by e.g. Papadakis et al. (2007); Edelson et al. (2002).

2.3 XMM-Newton

Ark 564 was observed by XMM-Newton from 2005 January 5, 19:47, to 2005 January 6, 23:16. The European Photon Imaging Cameras (EPIC) PN, MOS1 and MOS2 cameras were all operated in small window mode using a medium filter, as described by Papadakis et al. (2007). The total exposures for the PN and MOS cameras were 98.8 ks and 99.1 ks respectively. For the PN camera, we extracted source photons from a $\sim 2' \times 2'$ region and the background was selected from a source-free region of equal area on the same chip. Only single and double events, with quality flag=0 were retained. For the MOS1 and MOS2 cameras, source photons were extracted from a circular region of $\sim 46''$ in radius and single, double, triple and quadruple events were used. The PN data was free of pile-up, but both MOS cameras suffered significant pile-up in the cores of the target PSFs. Therefore we discarded data from the central $12''$ diameter of each MOS exposure. The average PN background-subtracted count rate in the 0.2–10 keV band was ~ 28 c/s. The background level was low and almost constant throughout the observation.

We produced light curves in the 0.2–2 and 2–10 keV energy bands in 48 s bins, and combined the light curves from the different detectors to produce weighted average light curves. The 0.2–10 keV lightcurve is shown in Fig 1 (see also Papadakis et al. 2007). As the variability properties normally depend on energy band, we also constructed XMM-Newton light curves from the PN data alone in the 0.5–2 and 2–8.8 keV bands, to match the average energies of the ASCA light curves. We used these lightcurves in all quantitative analyses.

3 ASCA POWER SPECTRUM

The superposed PSDs derived from the ASCA 2–10 keV and 0.6–2 keV data are shown in Fig. 2. Data below 10^{-4} Hz result from the light curves binned on the orbital time-scale. Data above $10^{-3.5}$ Hz are the sum of the PSDs derived from the many short sub-orbital light curves. Note the frequency gap that these data do not cover. The Poisson noise level has been subtracted. On time-scales longer than the orbital time-scale, the low and high energy PSDs have a similar normalisation. However on shorter time-scales the 2–10 keV

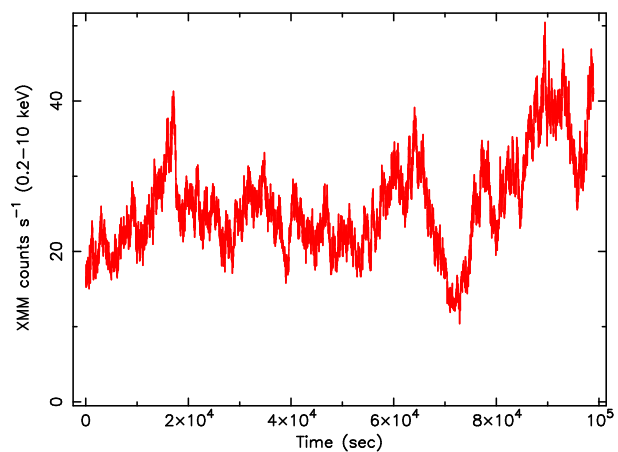


Figure 1. A weighted average combined PN, MOS1 and MOS2 XMM-Newton lightcurve in the 0.2–10 keV band.

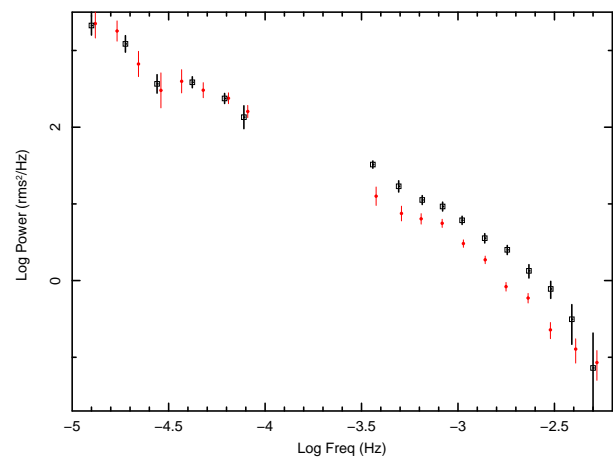


Figure 2. ASCA PSDs. The open (black) squares, with thick lines, are the 2–10 keV data. The filled (red) circles, with thin lines, are the 0.6–2 keV data. The Poisson noise level has been removed from both datasets. Data below 10^{-4} Hz result from lightcurves binned on the orbital time-scale. Data above $10^{-3.5}$ Hz are the sum of the PSDs derived from the many short sub-orbital lightcurves. The 2–10 and 0.6–2 keV data points have been shifted very slightly in frequency to avoid overlap at both ends of the overall PSDs.

PSD lies above the 0.6–2 keV PSD, except perhaps at the very highest frequencies ($\sim 10^{-2}$ Hz) where the two PSDs may be converging. This frequency dependent excess of the high energy PSD over the low energy PSD both below and above the high frequency break ($\sim 10^{-3}$ Hz), which is different from the behaviour of other well observed AGN, (e.g. NGC4051, M^cHardy et al. 2004), will be modelled properly in Section 5.

4 XMM-Newton POWER SPECTRUM

The XMM-Newton light curves were almost completely continuous except for 5 small gaps of duration 20–30 secs

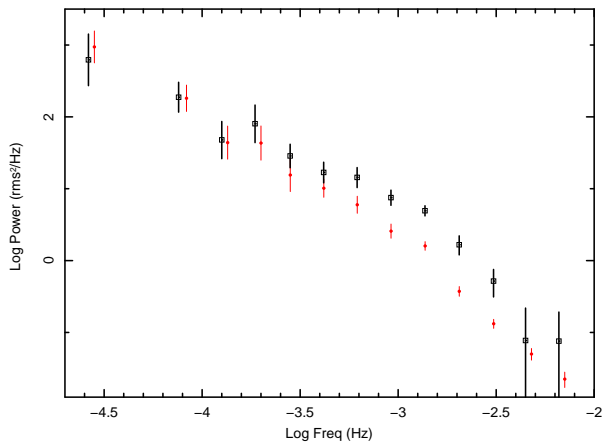


Figure 3. *XMM-Newton* PSDs. Here, for display purposes, we show the 2–10 keV (upper data points, black open squares, thick lines) and 0.2–2 keV (lower, red filled circles, thin lines) PSDs, with Poisson noise level subtracted, as the band centroids are more separated than for the 0.5–2 and 2–8.8 keV bands. Thus spectral differences, particularly the excess around 10^{-3} Hz at higher energies, are a little more pronounced. We do, however, use the 0.5–2 and 2–8.8 keV bands (Table 1) for quantitative analyses, to match better the *ASCA* energy bands.

each. Following the procedure established in McHardy et al. (2004) these gaps were filled by linear interpolation, together with the addition of noise characteristic of the surrounding data points, in order to eliminate spurious high frequency power in the power spectrum. Power spectral densities were derived from these light curves using a standard direct Fourier transform. In Fig. 3 we show the 0.2–2 and 2–10 keV PSDs and we see close agreement with the *ASCA* PSDs in the same energy bands. As with the *ASCA* PSDs, the low and high energy *XMM-Newton* PSDs coincide very closely at frequencies below 10^{-4} Hz, but at higher frequencies the 2–10 keV PSD exceeds the lower energy PSD. Note that here, for the low energy band, we show the 0.2–2 keV PSD rather than the 0.5–2 keV PSD and note that the bump centred around 10^{-3} Hz is even less pronounced in the 0.2–2 keV band, strengthening our observation that the excess has a strongly energy-dependent shape. Although not shown, the *XMM-Newton* 0.5–2 keV PSD is almost identical to the *ASCA* 0.6–2 keV PSD.

A simple power law fit to both low and high energy PSDs is a very poor fit, leaving a large residual bump centred around 10^{-3} Hz. A bending powerlaw, however, which provides a good fit to the high/soft state of Cyg X-1 and to the *XMM-Newton* PSDs of NGC4051 (McHardy et al. 2004) and MCG-6-30-15 (McHardy et al. 2005), is a good fit (Table 1). Tying the break frequencies to be the same in both energy band PSDs, we note (as can also be seen directly from Fig. 3), that although the slopes above the break are similar in both energy bands, the slope below the break is noticeably flatter at higher energies. The *ASCA* PSDs, although less well defined because of the gap on the orbital time-scales, are quite consistent with the fit parameters given in Table 1. This behaviour is different from that of NGC4051 and MCG-6-30-15 (e.g. see Table 6 of

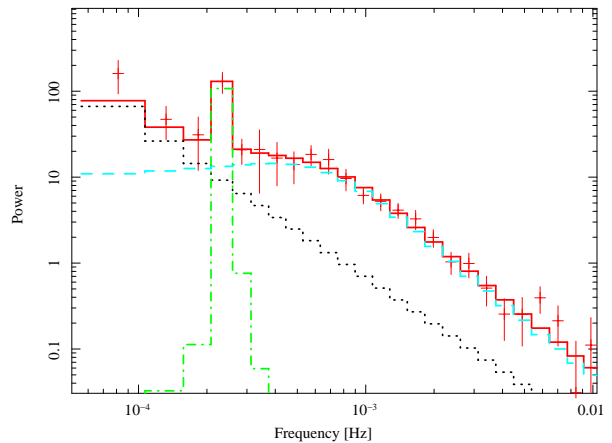


Figure 4. *XMM-Newton* 2–8.8 keV *XMM-Newton* PSD showing the model components. The broad high frequency Lorentzian is shown by a dash (light blue) line, the narrow Lorentzian is shown by a dot-dash (green) line, the underlying power law component is a dotted (black) line, the data points are (red) crosses, and the overall model is a solid (red) line. The Poisson noise level has been subtracted.

McHardy et al. 2005) where, although the slopes below the break are not very well determined, there is no evidence for a variation with energy. Above the break, however, the slope is flatter at higher energies in NGC4051 and MCG-6-30-15.

The PSD slope variations seen here in Ark 564 can be more naturally interpreted in terms of a power law (which is necessary to explain the power at low frequencies) together with a Lorentzian component which is stronger at higher energies. Such a model, in which the power law slope and normalisation, and Lorentzian central frequency are tied, provides an equally good fit to the data. In the case of the latter model, we note that the Lorentzian component is approximately three times stronger in the 2–8.8 keV than 0.5–2 keV band (Table 2). An increasing Lorentzian amplitude at higher energies is also typically observed in QPOs and some broad Lorentzian components in GBHs (e.g. Pottschmidt et al. 2003). As the exact values of the fit parameters depend on proper fitting of the lower frequency data from *RXTE* and *ASCA* we leave further discussion to Section 5.

There is a residual to the power law plus Lorentzian fit to the *XMM-Newton* PSD at $\sim 2.2 \times 10^{-4}$ Hz. This residual can be fitted (using the unbinned data) by the addition of a second, narrow (width $\sim 8 \times 10^{-6}$ Hz), Lorentzian with normalisation approximately half that of the broad Lorentzian. The fit is shown in Fig. 4. The fit is improved but, adjusting the F-test probabilities to take account of the fact that the line could have appeared in any of the available frequency bins, we find that the improvement is significant only at the 90% confidence level.

Table 1. Bending Powerlaw: combined fit to the XMM-Newton soft and hard band data

Energy Band keV	α_{mid}	α_{high}	ν_B Hz	red χ^2	d.o.f
0.5–2	1.31 ± 0.12	3.62 ± 0.37	$1.73 \pm 0.44 \times 10^{-3}$		
2.0–8.8	0.95 ± 0.14	3.57 ± 0.61	tied	0.88	37

Table 2. Power Law with Lorentzian Line: combined fit to the XMM-Newton soft and hard band data

Energy Band keV	α	Line centre Hz	Line width	Line normalisation	red χ^2	d.o.f
0.5–2.0	1.80 ± 0.19	$3.94 \pm 1.7 \times 10^{-4}$	$6.8 \pm 16 \times 10^{-4}$	$8.8 \pm 5.7 \times 10^{-3}$		
2.0–8.8	tied	tied	$1.1 \pm 0.17 \times 10^{-3}$	$24.1 \pm 8.4 \times 10^{-3}$	1.05	35

5 COMBINED XMM-Newton, ASCA AND RXTE POWER SPECTRA

The *RXTE* data, which covers time-scales from ~ 3 years to 3 hours, has already been analyzed by Pounds et al. (2001) and, including further data, by Markowitz et al. (2003) who both fit a breaking power law model to the PSD. Markowitz et al. (2003) derive a slope at the lowest frequencies α_L of $0.05_{-2.05}^{+0.55}$, a break frequency, $\nu_L = 1.59_{-0.95}^{+4.73} \times 10^{-6}$ Hz and an intermediate slope above the break of $\alpha_I = 1.20_{-0.35}^{+0.25}$. The earlier results of Pounds et al. (2001) are consistent with these values. We begin by refitting these data using our standard simulation-based modelling method (e.g. see Uttley et al. 2002). We fit a simple bending power law model (e.g. see M^cHardy et al. 2004, 2005). We bin the long time-scale *RXTE* light curve into 4-d bins, and the short time-scale *RXTE* light curve into 3-h bins. The resultant best-fitting values are similar to those of Markowitz et al. (2003) and the errors in the fit parameters are similarly large. As our value of α_L is quite consistent with zero and as, in both their hard and very high states, GBHs have $\alpha_L = 0$, we fix $\alpha_L = 0$ in subsequent power law fits.

5.1 Doubly-bending power law fit

We then fit the combined *RXTE*, *ASCA* and *XMM-Newton* data sets with a doubly bending power law model, including a second, higher frequency break at ν_H and slope α_H at the highest frequencies. We include the *ASCA* 2–10 keV SIS data in 512s bins and the *XMM-Newton* PN data in 48s bins in the 2–8.8 keV band to match the average energy of the *ASCA* band. The PN bin value was chosen so that the resultant light curve has 2^{11} points so that we can use the fast Fourier transform, rather than the slower direct Fourier transform, for that part of the simulation, without loss of accuracy.

We obtain a very good fit (acceptance probability $P=75\%$ - see Table 3 and Fig. 5) with $\alpha_I = 1.2_{-0.1}^{+0.2}$, $\nu_L = 7.5_{-5.5}^{+28.1} \times 10^{-7}$ Hz and $\nu_H = 2.4_{-0.9}^{+2.3} \times 10^{-3}$ Hz. These break frequencies are in good agreement with the values obtained by Papadakis et al. (2002) from analysis of *ASCA* data.

In order to make a combined PSD fit of the soft X-ray band, we first compared the low frequency variability power

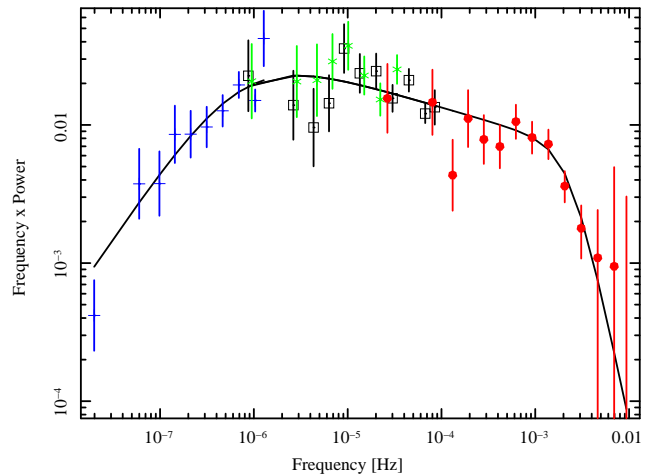


Figure 5. PSD of Ark 564 from *RXTE*, *ASCA* and *XMM-Newton* data in the 2–10 keV *RXTE* energy band. The solid black line shows the best-fitting double-broken power law model. The symbols with error bars represent the data, unfolded from the distortions of the observational sampling pattern. The crosses (blue) are from the *RXTE* 4-d sampling lightcurve, the asterisks (green) are from the *RXTE* 3-h sampling lightcurve, the open squares (black) are from the *ASCA* 2–10 keV SIS 512s-binned lightcurve and the filled circles (red) are from the 48s-binned *XMM-Newton* 2–8.8 keV PN data.

of the *ASCA* SIS data in the 0.6–2 and 2–10 keV bands. The resultant power spectra showed identical amplitudes, so both energy bands can be fit together at low frequencies without needing to rescale their PSDs. We assume that the close similarity of the 0.6–2 and 2–10 keV lightcurves continues to even lower frequencies, i.e. those sampled by the *RXTE* long term data. We therefore fitted the *RXTE* 2–10 keV long term data together with the SIS and *XMM-Newton* 0.6–2 keV data to cover the same frequency range as above. The fit is again very good ($P=85\%$ - Table 3) giving parameters $\alpha_I = 1.5_{-0.4}^{+0.1}$, $\nu_L = 3.6_{-2.9}^{+5.1} \times 10^{-6}$ Hz and $\nu_H = 1.8_{-1.4}^{+1.8} \times 10^{-3}$ Hz. The steeper intermediate slope reflects the lower high-frequency power in the soft band compared to the hard band. The break frequencies in both bands are consistent within 1σ uncertainties, as can be seen from the confidence contours plotted in Fig. 6

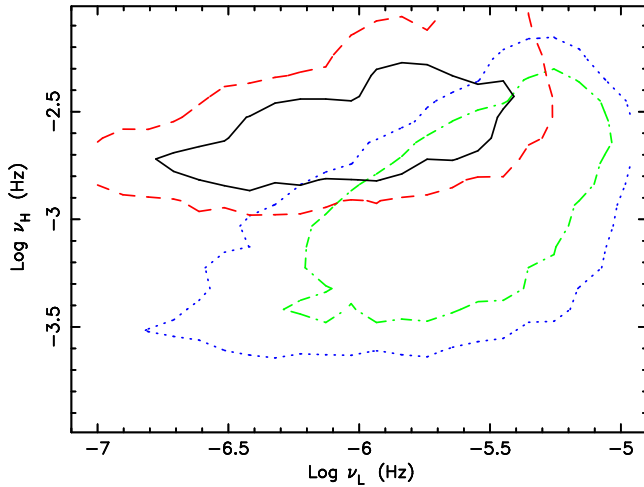


Figure 6. 68 % and 90 % confidence contours for high and low bend frequencies of the doubly-bending model fit to the combined PSD. Hard band contours (black and red respectively) are plotted in solid and dashed lines, soft band contours (green and blue respectively) in dot-dashed and dotted lines.

5.2 Double Lorentzian fit to the power spectrum

Motivated by the strong evidence for a Lorentzian component in the *XMM-Newton* data alone, we have fitted the combined *RXTE*, *ASCA* and *XMM-Newton* data with a model consisting of two Lorentzian components,

$$P(\nu) = A_L \frac{Q_L \nu_{c,L}}{\nu_{c,L}^2 + 4Q_L^2(\nu - \nu_{c,L})^2} + A_H \frac{Q_H \nu_{c,H}}{\nu_{c,H}^2 + 4Q_H^2(\nu - \nu_{c,H})^2} \quad (1)$$

where the Lorentzian peak frequency ν_{peak} is related to the centroid frequency ν_c by $\nu_{\text{peak}} = \nu_c(1 + 1/4Q^2)^{1/2}$ and the subscripts L and H refer to the low and high frequency components, respectively. We fitted the combined PSD in soft and hard energy bands independently, allowing all parameters to vary. The low frequency component converged to very low values of the quality factor $Q = \nu_c/\Delta\nu_{\text{FWHM}}$, i.e. to very wide Lorentzians where the Lorentzian shape is almost insensitive to the value of Q . We therefore fixed this parameter at $Q = 0.01$ (with 90% and 99% upper confidence limits of $Q = 0.2$ and 0.5 respectively) for both energy bands to enable a more detailed parameter grid search for the other parameters, and hence to obtain better constraints on these parameters. The best-fitting values are listed in Table 3. The Lorentzian peak frequencies are similar to, but not exactly the same as, the corresponding break frequencies, with the Lorentzian frequencies lying closer to the centre of the band-limited power.

Figures 7 and 8 show the best-fitting two-Lorentzian models to the hard and soft band respectively. In this interpretation, the increase in variability power at high frequencies in the hard band is entirely due to the greater strength of the high frequency Lorentzian in this band. The peak frequencies in both energy bands are consistent within the 90% confidence limits (see contour plot in Fig.9).

Note that Figs. 7 and 8 show the PSD unfolded through the distortions produced by sampling effects. These distor-

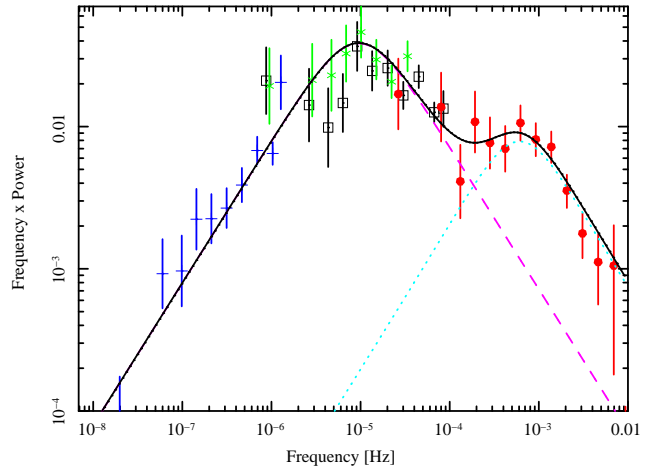


Figure 7. PSD of Ark 564 from *RXTE*, *ASCA* and *XMM-Newton* data in the 2–10 keV *RXTE* energy band. The dashed (red) line shows the low frequency Lorentzian, the dotted (blue) line shows the high frequency Lorentzian and the solid black line shows the best-fitting combined double Lorentzian model. The symbols with error bars, which are the same as in Fig. 5, represent the data unfolded from the distortions of the observational sampling pattern.

tions also depend on the underlying PSD shape so the resultant unfolded PSD depends on the model being fitted. If the two-Lorentzian model is the correct underlying PSD, the strong power component around 10^{-5} Hz will lead to spurious apparent power at lower frequencies in a PSD which has not been unfolded from the distortions, and where the low frequency part of the PSD has been derived from observations which do not sample the 10^{-5} Hz region. This effect is known as aliasing (e.g. see Uttley et al. 2002, for more details) and here particularly affects the long timescale *RXTE* data (blue crosses in Figs 5, 7 and 8). When we unfold the PSD we remove this spurious low frequency power. Thus the lowest frequency part of the PSDs in Figs. 7 and 8 lies below the same part in the bending power law model (Fig.5), where the model did not contain so much power at higher frequencies. Therefore the low break frequency in Fig. 5 is lower than in Figs. 7 and 8.

Since the normalisations of low and high-frequency Lorentzians are highly correlated with each other and with the Lorentzian frequency, we only treat the ratio of the low and high-frequency Lorentzian normalisations, A_L/A_H , as a free parameter and do not fit the high and low-frequency normalisations separately. Although the 1-dimensional errors quoted in Table 3 seem to indicate that the normalisation ratios for the hard and soft band overlap, we show in Fig. 10 that the 90% confidence contours of $\nu_{\text{peak,H}}$ versus A_L/A_H do not overlap. Therefore, for the same $\nu_{\text{peak,H}}$, the high-frequency Lorentzian is always relatively stronger, compared to the low-frequency Lorentzian, in the hard band than in the soft band. In fact, the low-frequency Lorentzian normalisation is similar in both bands and relatively well-constrained. For the best fitting model parameters, the values of fractional rms in the low frequency Lorentzian are $35 \pm 1\%$ and $33 \pm 1\%$ in hard and soft bands respectively,

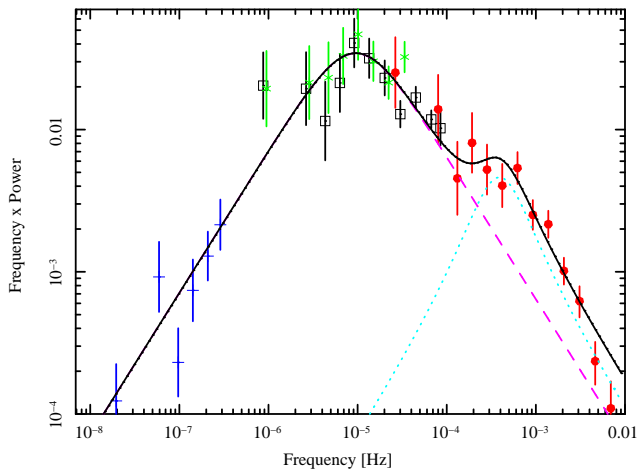


Figure 8. PSD of Ark 564 from *RXTE* in the 2–10 keV band and *ASCA* and *XMM-Newton* data in the 0.6–2 keV energy band. The solid line shows the best-fitting double Lorentzian model and symbols with errorbars, which are the same as in Fig. 5, represent the data, unfolded from the distortions of the observational sampling pattern.

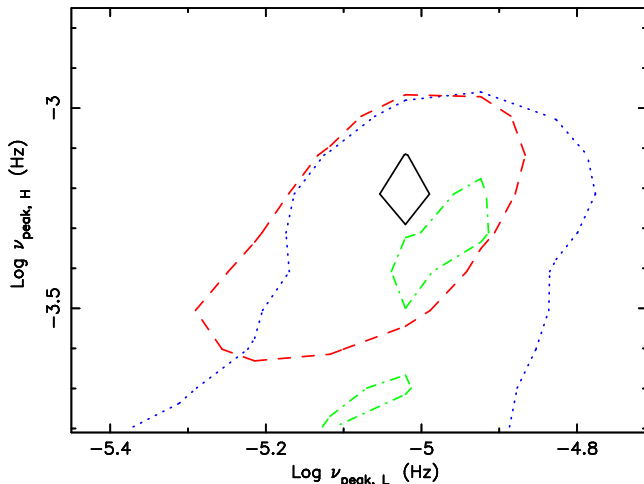


Figure 9. 68 % and 90 % confidence contours for high and low peak frequencies of the two-Lorentzian model fit to the combined PSD. Hard band contours are plotted in solid black and dashed red lines, soft band contours in dot-dashed green and dotted blue lines.

and in the high frequency Lorentzian the values are $15 \pm 1\%$ and $10 \pm 1\%$ in hard and soft bands. Thus the low frequency Lorentzian rms values are consistent with being the same, while the high frequency Lorentzian is weaker in the soft band, which explains the different hard and soft band PSD shapes at high frequencies.

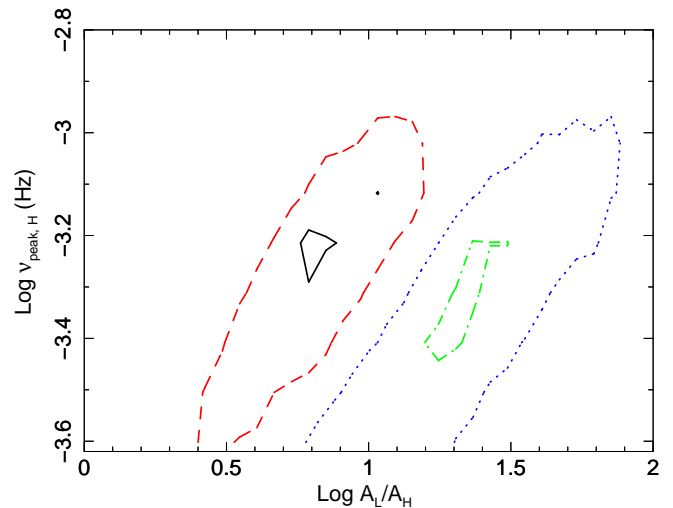


Figure 10. 68% and 90% contours for high-frequency Lorentzian peak frequency versus the ratio of low and high-frequency Lorentzian normalisations, A_L/A_H . Hard band contours are plotted in solid black and dashed red lines, soft band contours in dot-dashed green and dotted blue lines.

6 IMPLICATION OF LORENTZIAN PSD SHAPE ON TIME LAGS BETWEEN ENERGY BANDS

In Galactic black hole systems, lags are observed between light curves in different energy bands, with the higher energy variations generally lagging the lower energy variations (referred to here as a ‘positive’ lag). If the light curves in the different bands are separated into different Fourier components, it is generally found that the time lags between bands vary as a function of the Fourier frequency, i.e. time-scale, of the component, with larger lags being associated with longer time-scales. (See Nowak et al. (1999) for a full discussion of the relevant analysis techniques). Such lags have now been measured in some AGN (e.g Papadakis et al. 2001; M^cHardy et al. 2004), including in Ark 564 (Arévalo et al. 2006).

Arévalo et al. (2006) show that, for Ark 564, the positive time lag between the 0.5–2 and 2–8.8 keV *XMM-Newton* bands is approximately 800 s at low Fourier frequencies and ~ 0 s at high frequencies, with a sharp drop in time lag values at a frequency of $\sim 10^{-4}$ Hz. This stepped appearance of the lag spectrum resembles that seen in Cyg X-1 in the low/hard and intermediate states, where the steps in the lag spectrum correspond to the transition frequencies between peaks in the corresponding PSDs (Nowak et al. 1999; Nowak 2000). The correspondence between lag spectrum steps and PSD peaks suggests that each constant-lag value is associated with a given variability component, seen as a Lorentzian component in the PSD. Therefore, the shape of the lag spectrum in Ark 564 suggests that the two-component interpretation of the PSD is correct.

Table 3. Fit to the PSD using combined *XMM-Newton*, *ASCA* and *RXTE* data

Doubly-bending power law						
Energy Band	ν_L [Hz]	ν_H [Hz]	α_L	α_I	α_H	fit probability
0.6–2.0	$3.6^{+5.1}_{-2.9} \times 10^{-6}$	$1.8^{+1.8}_{-1.4} \times 10^{-3}$	0.0	$1.5^{+0.1}_{-0.4}$	3.4^{+*}_{-1}	0.85
2.0–8.8	$7.5^{+28.1}_{-5.5} \times 10^{-7}$	$2.4^{+2.3}_{-0.9} \times 10^{-3}$	0.0	$1.2^{+0.2}_{-0.1}$	$4.2^{+*}_{-1.8}$	0.75

Two-Lorentzian model						
Energy Band	low- ν Lorentzian		high- ν Lorentzian		A_L/A_H	fit probability
	$\nu_{\text{peak,L}}$ [Hz]	Q_L	$\nu_{\text{peak,H}}$ [Hz]	Q_H		
0.6–2.0	$9.5^{+2.4}_{-1.9} \times 10^{-6}$	0.01	$3.9^{+2.2}_{-2.3} \times 10^{-4}$	$0.5^{+0.5}_{-0.38}$	$17.6^{+290.4}_{-11.9}$	0.37
2.0–8.8	$9.5^{+2.0}_{-1.5} \times 10^{-6}$	0.01	$6.1^{+1.5}_{-1.3} \times 10^{-4}$	$0.125^{+0.38}_{-*}$	$6.15^{+4.7}_{-1.0}$	0.40

* The errors are large and are not very well defined.
All errors are 68% confidence (1σ).

6.1 Fitting the two-Lorentzian model jointly to the PSD and lag spectra

To test the above hypothesis we directly fitted the lag spectrum with a model corresponding to the lags expected from two Lorentzian variability components, each with a single distinct time lag, which is constant for all Fourier frequencies. The observed lag at any particular frequency is then a function of the overlap between the two Lorentzians, and must be calculated in the complex Fourier domain, by evaluating the cross-spectrum as a function of Fourier frequency, ν . The cross-spectrum is given by $C(\nu) = S(\nu)H^*(\nu)$, where $H(\nu)$ and $S(\nu)$ are the Fourier transforms of the hard and soft band light curves and the asterisk denotes the complex conjugate. $S(\nu) = S_l(\nu) + S_h(\nu)$ where the subscripts l and h denote the low and high-frequency Lorentzians respectively, and similarly for the hard band, $H(\nu) = H_l(\nu) + H_h(\nu)$. For the low and high frequency Lorentzian components, the soft band light curve is correlated with the hard band light curve except with a phase lag $\phi_l(\nu)$, $\phi_h(\nu)$ respectively. We determine the phase lag from the fixed low and high-frequency Lorentzian *time* lags τ_l and τ_h , by using $\phi(\nu) = 2\pi\nu\tau$. To avoid clutter, we now drop the frequency-dependence of the various parameters and write the real part of the cross-spectrum as follows:

$$Re(C) = Re(S) \times Re(H) + Im(S) \times Im(H) \quad (2)$$

$$= [Re(S_l) + Re(S_h)][Re(H_l) + Re(H_h)] + [Im(S_l) + Im(S_h)][Im(H_l) + Im(H_h)] \quad (3)$$

$$= [|S_l| \cos(\phi_0 + \phi_l) + |S_h| \cos(\phi_1 + \phi_h)] \times [|H_l| \cos(\phi_0) + |H_h| \cos(\phi_1)] + [|S_l| \sin(\phi_0 + \phi_l) + |S_h| \sin(\phi_1 + \phi_h)] \times [|H_l| \sin(\phi_0) + |H_h| \sin(\phi_1)], \quad (4)$$

where Re and Im denote real and imaginary components. ϕ_0 and ϕ_1 are simply random phase values for the low and high frequency Lorentzians respectively, measured for each realisation of the light curves, and will be different for different realisations. They are not related to the phase lags of interest between bands, i.e. ϕ_l and ϕ_h for the low and high frequency Lorentzians. For a noise process, such as the broad Lorentzians observed here, ϕ_0 and ϕ_1 , in indepen-

dent Fourier frequencies, are independently and identically distributed over a uniform distribution between 0 and 2π . The coefficients of the cross terms $|S_l||H_h|$ and $|H_l||S_h|$ will average to 0 when taking the average value of the cross spectrum for many realizations of the light curves, or many frequencies within a frequency bin, and the average value of $Re(C)$ is then

$$\langle Re(C) \rangle = |S_l||H_l|\langle \cos \phi_l \rangle + |S_h||H_h|\langle \cos \phi_h \rangle \quad (5)$$

Similarly we can show that $Im(C)$ is given by

$$\langle Im(C) \rangle = |S_l||H_l|\langle \sin \phi_l \rangle + |S_h||H_h|\langle \sin \phi_h \rangle \quad (6)$$

$|S_l|$, $|H_l|$, $|S_h|$ and $|H_h|$ correspond to the square root of the power of those Lorentzians in each energy band, at the frequency bin to be evaluated. The observed phase lag is simply the argument of the cross-spectrum, so the observed frequency-dependent time lag, $\tau(\nu)_{obs}$ can be evaluated from equations 5 and 6 using:

$$\tau(\nu)_{obs} = \frac{1}{2\pi\nu} \tan^{-1} \frac{Im(C(\nu))}{Re(C(\nu))}. \quad (7)$$

which can be fitted directly to the observed lag spectrum using the best-fitting Lorentzian PSD model obtained in Section 5.2 and letting the low and high-frequency time lags be free parameters. This simple model reproduces well the shape of the observed lag spectrum, shown in Fig. 11, with a reduced $\chi^2 = 1.35$ for 17 d.o.f (fit probability=0.15). The best-fitting values are 638 ± 54 s for the low-frequency lag and -11.0 ± 4.3 s for the high-frequency lag.

The low frequency components fitted to the PSD data in both energy bands are identical, but the high frequency components had different Q and peak frequency values, although they agree at the 1σ level. Forcing the high frequency components to be equal in both energy bands, using $Q_h = 0.5$ and $\nu_{\text{peak,h}} = 6.1 \times 10^{-4}$ Hz (both within 1σ of the best-fitting values), produces a better fit to the lag spectrum, with reduced $\chi^2 = 1.13$ for 17 d.o.f. (fit probability = 0.32), and lags consistent with the previous fit. The consistency between the lag spectrum and PSD significantly strengthens the interpretation of the PSD of Ark 564 as the summation of Lorentzian components, and hence as a very high state system.

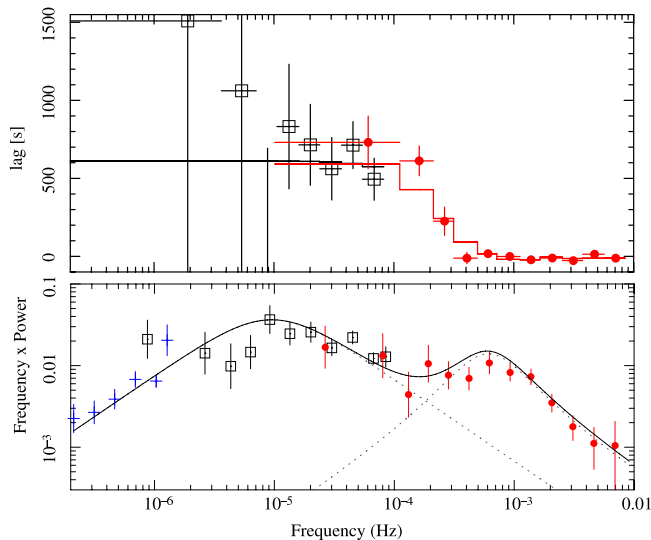


Figure 11. Top panel: Lag of soft (0.5–2 keV) band to hard (2–8.8 keV) band, as a function of frequency, calculated using *ASCA* and *XMM-Newton* data. The solid line represents the lag spectrum expected for a two-Lorentzian PSD model with the parameters obtained by fitting the PSD, forcing the Lorentzian components of the hard and soft bands to be equal. Each Lorentzian is assumed to have a constant time lag, whose values were obtained by fitting the lag spectrum, resulting in 638 ± 54 s (i.e. hard band lags) and -11.0 ± 4.3 s (hard band leads) for the low and high frequency Lorentzians, respectively. Bottom panel: hard band PSD as shown in Fig 7, with individual Lorentzian components overplotted. Note how the lags (top panel) are approximately constant in the frequency range when any one Lorentzian component dominates, and how the lags rapidly change in the frequency range where the dominance of individual Lorentzian components crosses over.

6.2 Coherence

The variability in the soft and hard bands is relatively coherent. Measuring the degree of linear correlation between energy bands as a function of Fourier frequency shows that the light curves remain coherent (coherence, γ^2 , ~ 0.8 where $\gamma^2 = 0$ for uncorrelated light curves and $\gamma^2 = 1$ for perfectly correlated light curves) up to frequencies of at least 10^{-3} Hz (see figure 3 in Arévalo et al. (2006)). The coherence is consistent with the two-component interpretation, even if the variability patterns of the low and high frequency Lorentzians are uncorrelated. For example, if one energy band is fully modulated by one of the Lorentzians, while at the same time-scales the other energy band responds equally to both Lorentzians, the coherence would drop to a value of $\gamma^2 = 0.5$. This extreme case never occurs in the present data, so the coherence can remain over 50 % even if the Lorentzians are uncorrelated. The relative contribution of the Lorentzians to each energy bands is most different at frequencies $\sim 2 \times 10^{-3}$ Hz, where both Lorentzians have similar power in the hard band (Figs.7 and 8), but the high-frequency Lorentzian is 10 times stronger than the low frequency component in the soft band. In this

case, the coherence is expected to drop to ~ 0.75 , as measured by Arévalo et al. (2006) (their figure 3).

It is possible that the low-frequency variability component that we fit to the PSD as a very broad Lorentzian actually contains more components. The available data, however, are not good enough to disentangle extra components in the low frequency PSD. Unfortunately the lag spectrum cannot help in this case as the long term monitoring was performed only by *RXTE*, which has a hard energy response. We are therefore unable to compute a lag spectrum between hard and soft bands as we have been able to on intermediate and short time-scales.

7 DISCUSSION

7.1 Summary of PSD and lag fits

We have fitted the PSD of Ark 564 over the $10^{-8} - 10^{-2}$ Hz frequency range, combining long term archival *RXTE* monitoring data, a month-long observation by *ASCA* covering intermediate frequencies and a new 100 ks observation by *XMM-Newton* which covers the shortest time-scales. We confirm the existence of two breaks in the PSD, which make this the only AGN so far observed to have band-limited variability.

The PSD can be fitted either with a double-bending power law, where the variability power drops at low and high frequencies, or with a combination of two distinct variability components, peaking close to the low and high frequency breaks, respectively. Using two Lorentzian-shaped components, we obtain a good fit in both the soft 0.5–2 and hard 2–10 keV bands, with self-consistent Lorentzian parameters between the energy bands. We note that, when fitting the upper break in the PSD, the frequency of the fitted Lorentzian is a factor of 4 lower than the fitted bend frequency as, in any band-limited PSD, the Lorentzian fits will tend to move towards the centre of the band. This difference should be considered when combining values of PSD break timescales derived from different fitting methods. In the Lorentzian interpretation of the PSD, the increase in variability power at high frequencies in the hard band is explained by a strengthening of the high frequency Lorentzian, as is seen in GBHs (e.g. Pottschmidt et al. 2003), while the low frequency Lorentzian remains approximately at the same level.

The two-component interpretation is strongly supported by the lag spectrum calculated between these energy bands using *ASCA* and *XMM-Newton* data (Arévalo et al. 2006). The lag spectrum has a step-like shape, where the time lags are approximately constant at low frequencies and drop sharply to a different constant value at around 10^{-4} Hz. The drop in the lag spectrum occurs exactly at the frequency expected if each Lorentzian component has a single time lag value associated with it. This characteristic lag spectral shape therefore provides strong evidence that the different Lorentzian components in the PSD arise from distinct physical regions, e.g. different radii in the accretion disc.

7.2 Scaling Relationships

The lag spectrum of Ark 564 has a very similar shape to that of Cyg X-1 in its intermediate state (see figure 8 of Arévalo et al. 2006), although the frequencies are, of course, very different. However our recent 3D fit (McHardy et al. 2006) shows that PSD break frequencies scale not only inversely with black hole mass, M , but also approximately with \dot{m}_E . If we apply the same scaling to the lag frequencies, then Ark 564 and Cyg X-1 in its intermediate state coincide almost exactly.

Ark 564 was included in our 3D fit, using the value of T_B given by Papadakis et al. (2002), and lay close to the best-fitting plane. The better measured value of T_B which we derive here, on the assumption of a bending power law, is identical to the value of T_B given by Papadakis et al. (2002) thus Ark 564 remains consistent with our previous scaling relationship.

All previous studies of the scaling between AGN and GBHs have concentrated on the high frequency part of the PSDs as the (scaled) low frequency part of most AGN PSDs is not well measured. On the basis of just one AGN where we are able to fit a low frequency Lorentzian component we are therefore extremely cautious in any comparison, and we also note that intermediate state GBH PSDs show many and varied shapes where the separation between high and low frequency Lorentzians is not constant (e.g. Axelsson et al. 2005, 2006; Belloni et al. 2005). However the separation of approximately 1.5 decades in frequency between the two Lorentzians seen here is not wildly different from typical separations seen in intermediate state GBHs. Thus some sort of mass (and probably also accretion rate) related scaling probably applies to the lower, as well as to the upper, PSD frequencies.

7.3 Radio luminosity and ‘state’

The PSD and lag spectrum indicate a VHS/intermediate state, rather than a soft state, with a hard state being ruled out because of the very high accretion rate. Is this state classification consistent with other state measures, e.g. radio luminosity? VHS/intermediate state GBHs can be quite luminous, although transient, radio sources (e.g. GRS1915+105, Miller-Jones et al. 2005) whilst soft state GBHs are undetected in deep radio observations.

Ark 564 (black hole mass $M \sim 2.6 \times 10^6 M_\odot$, Botte et al. 2004) is considerably more radio luminous than AGN with well defined soft-state PSDs and similar black hole masses, e.g. NGC4051 ($1.9 \times 10^6 M_\odot$, Peterson et al. 2004) and MCG-6-30-15 ($4.5 \times 10^6 M_\odot$, McHardy et al. 2005). Both NGC4051 (McHardy et al. in preparation; see also Christopoulou et al. 1997) and Ark 564 (Lal et al. 2004; Schmitt et al. 2001) contain flat spectrum VLBI cores for which $L_{Rad-Ark564} \sim 600 \times L_{Rad-NGC4051}$ (assuming redshift-derived distances). These observations are certainly consistent with a VHS/intermediate state interpretation for Ark 564 although the present lack of radio detection of soft state GBHs prevents a more quantitative comparison.

If the same disc-jet coupling applies in NGC4051 and

Ark 564 and the radio luminosity of the jet scales as $\dot{m}^{1.4}$ (absolute, not Eddington, units; Blandford & Konigl 1979), then we would expect $L_{Rad-Ark564} \sim 100 \times L_{Rad-NGC4051}$ (deriving \dot{m} from Uttley & McHardy 2005). Thus it is not yet clear whether the higher radio luminosity of Ark 564 relative to NGC4051 is purely due to a higher accretion rate or to some difference in jet structure.

7.4 Physical origin of the high frequency Lorentzian timescale

If we take the Lorentzian peak frequency ($\sim 6 \times 10^{-4}$ Hz, i.e. 1666s, in the 2–8.8 keV band) as being the best measurement of the underlying physical process responsible for the sharp drop in power, we can consider what that timescale might correspond to. The dynamical time-scale around the Ark 564 black hole ($2.6 \times 10^6 M_\odot$) is considerably shorter than the Lorentzian peak time-scale, unless we assume that the time-scale arises far (few tens of R_g) from the black hole. There is evidence from the broad iron X-ray fluorescence lines (Fabian 2005) that the accretion disc often reaches down to $< 2R_g$, close to the innermost stable orbit of a maximally spinning black hole. If the Lorentzian peak time-scale arises from the inner edge of such a spinning black hole disc, it may well correspond to the viscous time-scale (assuming a viscosity parameter, $\alpha = 0.1$). In that case the ratio of disc scale height to radius, H/R , = 1.2, which is reasonable given the very high accretion rate.

7.5 Combined interpretation of PSD and lag spectrum

A possible interpretation of both the PSD and lag spectrum is that the variability originates mainly in two distinct regions. Note that by ‘variability’ we mean the source of the variations, not the source of the X-rays. The variability may be related to accretion rate fluctuations in the accretion disc. It is reasonable to assume that variability time-scales are larger at larger radii (e.g. Lyubarskii 1997). Once produced, variations would then propagate inwards and, on reaching the X-ray emitting region, would modulate the emission. It is also reasonable to assume that the emitted energy spectrum becomes harder towards smaller radii so, for example, the bulk of the 0.5–2 keV emission will be emitted from a larger radius than the bulk of the 2–10 keV emission. If the region responsible for most of the variability at low frequencies lies outside all of the X-ray emitting region, then the time lag between the soft and hard bands may represent the time taken for the fluctuations to propagate from the ‘soft’ to ‘hard’ emission region (e.g. see Kotov et al. 2001, Arévalo & Uttley 2006). If all of the frequencies in the low frequency variability component are produced in the same region, for example a narrow annulus of the disc, then all of those frequencies will have the same soft-hard lag.

If the source of the higher frequency variations lies within the X-ray emission region, e.g. between the soft and hard emission regions, then the high frequency variations will affect only the harder emission region and the

resultant X-ray variations will be stronger at higher energies, as we observe. In this scenario the predominantly softer, outer emission region, which is subject only to the slower variations, may form part, or possibly all, of the so-called ‘soft excess’, i.e. the excess in the energy spectrum below $\sim 2\text{keV}$ above an extrapolation of a power law to low energies. This softer region, although lying outside the harder emitting region is, however, probably still quite close (ie within $\sim 10R_G$ rather than $\sim 100R_G$) to the black hole. This scenario is consistent with the observations of Turner et al. (2001) and Brinkmann et al. (2007) of Ark 564. Turner et al. (2001) show that, on ~ 1 day time-scales, the soft excess emission from Ark 564 varies at least as much as the power law emission. Brinkmann et al. (2007) show, by fitting a combination of bremsstrahlung (not necessarily a physical bremsstrahlung component but simply to fit the ‘soft excess’) and power law components to 500s sections of the *XMM-Newton* data discussed here, that the ‘bremsstrahlung’ component at low energies (0.3–1 keV) is less variable than the power law component in the same band, and that the power law component at higher energies (3–10 keV) is more variable still. However a full understanding of how the soft excess is related to the rest of the X-ray emission, e.g. whether it might actually be caused by absorption (Gierliński & Done 2006) requires detailed frequency-resolved spectroscopy (e.g. see Papadakis et al. 2007; Revnivtsev et al. 2001) for which the present data are insufficient.

We finally comment on the negative phase lag, $-11.0 \pm 4.3\text{s}$, at the highest observable frequencies. As the high frequency X-ray variations at lower energies will also be produced at small radii, e.g. as the low energy tail of the harder emission region, there should be very little lag between the soft and hard emission, as we see. However the lag is negative, i.e. the hard band leads, in the higher frequency component. This observation suggests that the high-frequency variability in the soft band might arise from reflection/reprocessing within $\sim 1R_g$ of the illuminating hard X-ray source, implying the existence of cold gas close to the central X-ray source.

ACKNOWLEDGEMENTS

This work is based on observations with *XMM-Newton*, an ESA science mission with instruments and contributions directly funded by ESA Member States and the USA (NASA). IMcH and PA acknowledge support from STFC under rolling grant PP/D001013/1 and PU acknowledges support from an STFC Advanced Fellowship. We acknowledge redshift data from the NASA/IPAC Extragalactic Database.

REFERENCES

Arévalo P., Papadakis I. E., Uttley P., McHardy I. M., Brinkmann W., 2006, *MNRAS*, 372, 401
 Arévalo P., Uttley P., 2006, *MNRAS*, 367, 801

Axelsson M., Borgonovo L., Larsson S., 2005, *A&A*, 438, 999
 Axelsson M., Borgonovo L., Larsson S., 2006, *A&A*, 452, 975
 Belloni T., Homan J., Casella P., van der Klis M., Nespoli E., Lewin W. H. G., Miller J. M., Méndez M., 2005, *A&A*, 440, 207
 Blandford R. D., Konigl A., 1979, *ApJ*, 232, 34
 Botte V., Ciroi S., Rafanelli P., Di Mille F., 2004, *AJ*, 127, 3168
 Brinkmann W., Papadakis I. E., Raeth C., 2007, *A&A*, 465, 107
 Christopoulou P. E., Holloway A. J., Steffen W., Mundell C. G., Thean A. H. C., Goudis C. D., Meaburn J., Pedlar A., 1997, *MNRAS*, 284, 385
 Edelson R., Turner T. J., Pounds K., Vaughan S., Markowitz A., Marshall H., Dobbie P., Warwick R., 2002, *ApJ*, 568, 610
 Fabian A. C., 2005, *ApSS*, 300, 97
 Gierliński M., Done C., 2006, *MNRAS*, 371, L16
 Kotov O., Churazov E., Gilfanov M., 2001, *MNRAS*, 327, 799
 Lal D. V., Shastri P., Gabuzda D. C., 2004, *A&A*, 425, 99
 Lyubarskii Y. E., 1997, *MNRAS*, 292, 679
 Markowitz A., Edelson R., Vaughan S., Uttley P., George I. M., Griffiths R. E., Kaspi S., Lawrence A., McHardy I., Nandra K., Pounds K., Reeves J., Schurch N., Warwick R., 2003, *ApJ*, 593, 96
 Miller-Jones J. C. A., McCormick D. G., Fender R. P., Spencer R. E., Muxlow T. W. B., Pooley G. G., 2005, *MNRAS*, 363, 867
 McHardy I. M., Gunn K. F., Uttley P., Goad M. R., 2005, *MNRAS*, 359, 1469
 McHardy I. M., Koerding E., Knigge C., Uttley P., Fender R. P., 2006, *Nature*, 444, 730
 McHardy I. M., Papadakis I. E., Uttley P., Page M. J., Mason K. O., 2004, *MNRAS*, 348, 783
 Nowak M. A., 2000, *MNRAS*, 318, 361
 Nowak M. A., Vaughan B. A., Wilms J., Dove J. B., Begelman M. C., 1999, *ApJ*, 510, 874
 Papadakis I. E., Brinkmann W., Negoro H., Gliozzi M., 2002, *A&A*, 382, L1
 Papadakis I. E., Brinkmann W., Page M. J., McHardy I., Uttley P., 2007, *A&A*, 461, 931
 Papadakis I. E., Ioannou Z., Kazanas D., 2007, *ApJ*, 661, 38
 Papadakis I. E., Nandra K., Kazanas D., 2001, *ApJL*, 554, L133
 Peterson B. M., Ferrarese L., Gilbert K. M., Kaspi S., Malkan M. A., Maoz D., Merritt D., Netzer H., Onken C. A., Pogge R. W., Vestergaard M., Wandel A., 2004, *ApJ*, 613, 682
 Pottschmidt K., Wilms J., Nowak M. A., Pooley G. G., Gleissner T., Heindl W. A., Smith D. M., Remillard R., Staubert R., 2003, *A&A*, 407, 1039
 Pounds K., Edelson R., Markowitz A., Vaughan S., 2001, *ApJL*, 550, L15
 Remillard R. A., McClintock J. E., 2006, *ARAA*, 44, 49
 Revnivtsev M., Gilfanov M., Churazov E., 2001, *A&A*, 380,

520

- Romano P., Mathur S., Turner T. J., Kraemer S. B., Crenshaw D. M., Peterson B. M., Pogge R. W., Brandt W. N., George I. M., Horne K., Kriss G. A., Netzer H., Shemmer O., Wamsteker W., 2004, *ApJ*, 602, 635
- Schmitt H. R., Ulvestad J. S., Antonucci R. R. J., Kinney A. L., 2001, *ApJS*, 132, 199
- Summons D. P., Arevalo P., McHardy I. M., Uttley P., Bhaskar A., 2007, *ArXiv e-prints*, 704
- Turner T. J., Romano P., George I. M., Edelson R., Collier S. J., Mathur S., Peterson B. M., 2001, *ApJ*, 561, 131
- Uttley P., McHardy I. M., 2005, *MNRAS*, 363, 586
- Uttley P., McHardy I. M., Papadakis I. E., 2002, *MNRAS*, 332, 231